





# Enhanced dilepton emission from a phase transition in dense matter

Oleh Savchuk<sup>1,2,3,\*</sup> , Anton Motornenko<sup>3</sup> ,  
Jan Steinheimer<sup>3</sup> , Volodymyr Vovchenko<sup>3,4,5</sup> ,  
Marcus Bleicher<sup>6,7</sup>, Mark Gorenstein<sup>2,3</sup> and  
Tetyana Galatyuk<sup>1,8</sup>

<sup>1</sup> GSI Helmholtzzentrum für Schwerionenforschung GmbH, D-64291 Darmstadt, Germany

<sup>2</sup> Bogolyubov Institute for Theoretical Physics, 03680 Kyiv, Ukraine

<sup>3</sup> Frankfurt Institute for Advanced Studies, Giersch Science Center, D-60438 Frankfurt am Main, Germany

<sup>4</sup> Institute for Nuclear Theory, University of Washington, Box 351550, Seattle, WA 98195, United States of America

<sup>5</sup> Nuclear Science Division, Lawrence Berkeley National Laboratory, 1 Cyclotron Road, Berkeley, CA 94720, United States of America

<sup>6</sup> Goethe-Universität Frankfurt, Institut für Theoretische Physik, Max-von-Laue-Str. 1, 60438 Frankfurt am Main, Germany

<sup>7</sup> Helmholtz Research Academy Hesse (HFHF), GSI Helmholtzzentrum für Schwerionenforschung GmbH, Campus Frankfurt, 60438 Frankfurt am Main, Germany

<sup>8</sup> Technische Universität Darmstadt, 64289 Darmstadt, Germany

E-mail: [savchuk@fias.uni-frankfurt.de](mailto:savchuk@fias.uni-frankfurt.de)

Received 17 April 2023, revised 29 August 2023

Accepted for publication 25 September 2023

Published 25 October 2023



CrossMark

## Abstract

It is demonstrated that the presence of a phase transition in heavy-ion collisions, at beam energies that probe dense quantum chromodynamics (QCD) matter, leads to a significant enhancement of the dilepton yield at low invariant mass and requires the embedding of low beam energies per produced pion due to the extended emission time. In addition, the temperature of low-mass dileptons shows a modest decrease due to the mixed phase. The emission of dileptons in the SIS18–SIS100 beam energy range is studied by augmenting the ultra-relativistic quantum molecular dynamics (UrQMD) transport model

\* Author to whom any correspondence should be addressed.



Original content from this work may be used under the terms of the [Creative Commons Attribution 4.0 licence](https://creativecommons.org/licenses/by/4.0/). Any further distribution of this work must maintain attribution to the author(s) and the title of the work, journal citation and DOI.

with a realistic density-dependent equation of state, as well as two different phase transitions. This is achieved by extending the molecular dynamics interaction part of the UrQMD model to a density-dependent interaction potential with a high-density minimum, leading to a phase transition and metastable coexisting high-density states. Together with a high-precision measurement, these simulations will be able to constrain the existence of a phase transition in QCD up to densities of several times nuclear saturation density.

Keywords: dileptons, SIS18, SIS100, phase transition, dense nuclear matter

(Some figures may appear in colour only in the online journal)

## 1. Introduction

The high-density structure of the quantum chromodynamics (QCD) phase diagram is one of the major challenges in theoretical and experimental high-energy physics. Relativistic heavy-ion collisions (HICs) probe different regimes of QCD matter by varying the collision energy and mass of colliding nuclei. Complementarily, the low-temperature and high-density region of the phase diagram is probed by neutron stars and, since the detection of the GW170817 gravitational wave event and its electromagnetic counterpart [1, 2], by their mergers. At vanishing net-baryon density, first-principle lattice QCD simulations show a smooth chiral crossover [3–5], which can be probed by the vast amount of data collected from HICs at the highest energies, e.g. at the large hadron collider (LHC) and relativistic heavy-ion collider (RHIC) [6–9]. On the other hand, the properties of matter at high and even intermediate net-baryon densities are still mostly unconstrained, and the existence of a first-order phase transition, with its corresponding critical endpoint, in this region is not ruled out. Besides the constraints from astrophysical observations of compact stars, one can only rely on signatures of a phase transition in HICs. Here, the challenge is to make unambiguous predictions for current and future experiments, which requires the embedding of a first-order phase transition into the hitherto existing models for the dynamical description of HICs.

Several experimental signals have been suggested as sensitive probes for the phase structure of the matter created in HICs. For example, the collapse of the directed flow [10–13], fluctuations and correlations [6, 14–17], as well as light nuclei enhancement [18], just to name a few. The experimental confirmation of these signatures is challenging, and no final conclusion has been reached so far. It is important to note that such signals cannot be interpreted isolated from the wealth of data that is now available and, in the end, only a fully consistent combination of observables can lead to conclusions on the phase structure and the dense matter equation of state (EoS).

Electromagnetic probes, in particular measurements of dilepton emission, are a promising tool for studying the properties of dense and hot matter [19–22]. They are of particular elegance compared to hadronic observables, as the hot hadronic medium is virtually transparent for electroweak interactions [23]. Hence, dileptons reflect the properties of the medium at the time and place of their emission. Inclusive dilepton spectra represent cumulative properties of the system at different times in its evolution. In collisions that create baryon-rich matter, one expects great sensitivity of the electromagnetic probes to the hadronic EoS and a possible phase transition [23–25]. At collisions in the vicinity of the phase transition, the strongest effect is expected from the slowed expansion, resulting in an extended lifetime that

consequently leads to a longer emission [20, 26, 27]. Dynamical simulations have shown this effect qualitatively for dileptons [25] and recently a full 3 + 1D ideal fluid dynamic simulation has confirmed this effect in a quantitative more realistic simulation, which predicted an increased emission of dileptons up to a factor of 2 [28]. On the other hand, it was discussed that the existence of a partonic phase can also lead to an enhancement of real photons at Supur Proton Synchrotron (SPS) and facility for antiproton and ion research (FAIR) energies [29].

The present work shows how the inclusion of a phase transition in dense QCD matter influences the total measured dilepton yield in the whole SIS18–SIS100 beam energy range. To make quantitative and realistic predictions we use a microscopic transport model, which naturally includes viscosity and finite size effects. In the following, it is shown how the well-tested UrQMD transport code can be modified to include a density-dependent first-order phase transition based on a many-body interaction potential. Predictions for possible dilepton measurements, sensitive to the phase transition and in particular on the extended lifetime in a realistic scenario, are then presented.

## 2. Dynamical description of HICs with a phase transition

An estimate of the dilepton emission from the rapidly expanding fireball of a relativistic HIC requires a detailed microscopic description of said evolution. For this, we will employ the well-known and tested UrQMD hadronic transport model in its most recent version (v3.5) [30–32]. It is based on the explicit propagation of hadrons in phase space, their two-body scatterings, and the decays of unstable particles. The imaginary part of the interactions is included through binary elastic and inelastic collisions (the latter leading mainly to resonance excitations and decays at the energies considered in the work, or color flux-tube formation and their fragmentation at higher energies). The real part of the interaction potential is implemented via a density-dependent single-particle potential  $U(n_B)$ . Using the single-particle potential, the mean-field potential energy  $V(n_B)$  at density  $n_B$  can be calculated to solve the classical equations of motions. Traditionally, the field energy per baryon is computed using a simple Skyrme potential [30, 33]. However, recently it was shown how a more sophisticated relativistic chiral mean-field model (CMF) can also be incorporated [34]. In the following, the CMF EoS in UrQMD will be used, as well as two modifications of the CMF EoS that produce phase transitions at high baryon densities, with a focus on studying the effect of the phase transitions on the dilepton emission in the SIS100 energy regime in a consistent approach. For previous dilepton studies within UrQMD we refer the reader to [35–37].

### 2.1. The equations of state

Baryon interaction dynamics in our approach consist of two contributions: (i) consecutive two-body scatterings and (ii) density-dependent potential. The latter does include finite-range many-body interactions. While we do not incorporate explicit three-body scatterings, to our knowledge, it has never been shown unambiguously that their introduction leads to significant changes in the dynamics [38, 39].

The treatment of the density-dependent potential in UrQMD as well as the construction and motivation for the phase transitions used in the following has been described in more detail in [40]. In the following, we will simply give a short summary and refer the interested reader to the above paper. As a baseline for the density-dependent EoS we use the CMF model in its most recent version [41]. The CMF model incorporates a realistic description of nuclear matter with a nuclear incompressibility of  $K_0 = 267$  MeV, chiral symmetry breaking in the hadronic and quark sectors, as well as an effective deconfinement transition. Recently it

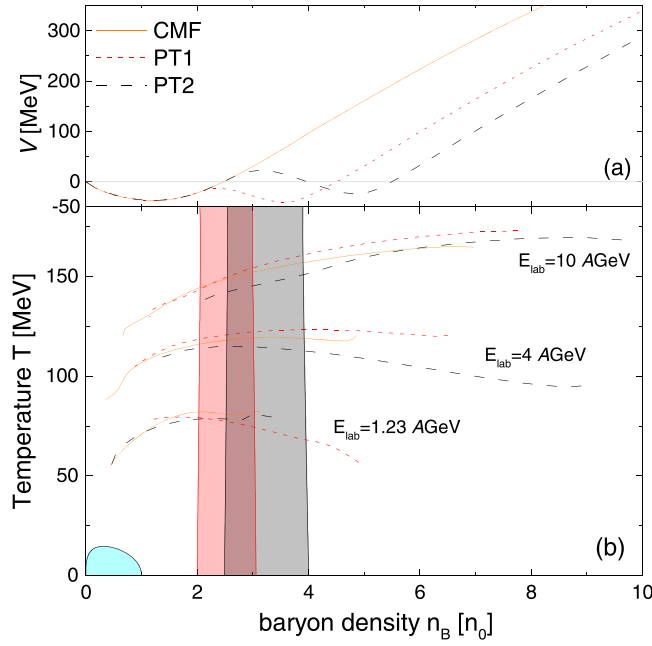


**Figure 1.** (a) The effective potential of baryons as a function of the baryon density  $n_B$  for all three EoS. The standard CMF version monotonously increases at higher densities, while the PT1 and PT2 scenarios incorporate additional phase transitions, which are represented by the secondary minima. (b) The event-averaged trajectories of the central cell are shown as calculated using the coarse-graining method for different beam energies. The spinodal regions of PT1 and PT2 in the  $n_B$ - $T$  phase diagram are indicated by the shaded regions.

was shown how the CMF EoS can be effectively implemented into the QMD equations of motion of the UrQMD model [34]:

$$\begin{aligned} \dot{\mathbf{p}}_i &= -\frac{\partial H}{\partial \mathbf{r}_i} = -\frac{\partial V}{\partial \mathbf{r}_i} \\ &= -\left( \frac{\partial V_i}{\partial n_i} \cdot \frac{\partial n_i}{\partial \mathbf{r}_i} \right) - \left( \sum_{j \neq i} \frac{\partial V_j}{\partial n_j} \cdot \frac{\partial n_j}{\partial \mathbf{r}_i} \right), \end{aligned} \quad (1)$$

where  $H$  is the total Hamiltonian and  $V = \sum_j V[n_B(r_j)]$  is the total potential energy of the system<sup>9</sup>. The potential derivative in equation (1) is calculated by summing over all possible baryon pairs  $j \neq i$ .  $V_i$  corresponds to the potential energy of a baryon at position  $r_i$ , and the local interaction density  $n_k$  at position  $r_k$  is calculated assuming that each particle can be treated as a Gaussian wave packet [30, 42].

In addition to the derivative of the mean-field potential energy per baryon  $\partial V(n_B)/\partial n_B$  that is used as input to UrQMD, only the local densities and gradients need to be calculated to solve the equations of motion for each baryon. The baseline CMF mean-field energy per baryon  $V(n_B)$  as a function of the baryon density is shown as an orange line in the upper panel of figure 1. The minimum around saturation density corresponds to the nuclear liquid–gas

<sup>9</sup> Here, momentum dependence is neglected.

transition; at higher density the potential monotonously increases due to the presence of repulsive interactions and the absence of any other phase transitions.

A simple augmentation is used in order to implement a phase transition in the CMF model [40]. To provide for another metastable state in the mean-field energy per baryon at large densities (in addition to the bound state from the nuclear liquid–gas transition), the original potential of CMF is cut at density  $n_B^{cut} = 2.1 n_0$  for PT1 and  $2.6 n_0$  for PT2.  $V(n_B)$  for  $n_B > n_B^{cut}$  is then shifted by  $\Delta n_B = 1.7 n_0$  and  $2.6 n_0$ , respectively.

The specific choice of the value for  $n_{cut}$  is motivated by two factors:

1. The transition should be reachable with HIC experiments (which limits the density range to  $n_B^{cut} < 4 - 5 n_0$ ) [34].
2. The density is higher than  $2 n_0$  to avoid discrepancies with available constraints from HICs and astrophysical observations [43].

Since the pressure consists not only of the potential but also the kinetic part, which increases with the density, an equal potential depth essentially means a higher pressure. Therefore, the high-density state of matter will coexist with a lower-density system but become unstable as soon as the density keeps decreasing due to the expansion of the low-density matter surrounding it.

The mean-field energy between  $n_B^{cut} < n_B < n_B^{cut} + \Delta n_B$  is then interpolated by a third-order polynomial in order to create a second minimum in energy per particle  $V(n_B)$  and ensure that its derivative is also a continuous function. There are infinite ways to create such a construction, each leading to different properties of the so-constructed transition. In [44], it was shown that the pressure that is obtained with such a density-dependent potential indicates instabilities beyond the spinodal line of a phase transition for which the baryon density is the order parameter. In addition, the derivatives of that pressure with respect to the chemical potential will diverge at the spinodal lines as expected for a first-order phase transition. For infinite systems we therefore expect the system to behave as it would undergo a first-order phase transition exactly. Since we are dealing with systems that are finite in space and time, one does not strictly obtain an exact phase transition, as there is always a finite probability that the system will be in either phase or a metastable state. Thus, we have checked in box simulations that indeed we obtain phase separation in clusters in the unstable region of our phase diagram as indicated in figure 1. It is therefore valid to claim that we are investigating the dynamics of interacting matter which, in the thermodynamic limit, would undergo a phase transition at the indicated densities. Other methods can be employed to construct high-density phase transitions; for example, using a vector density functional [45]. The goal of the present work is to study general signatures of a significant phase transition in the SIS100 energy regime, so we chose to add a significant dip in the potential for densities that are low enough to be reached by HICs at the SIS18/SIS100 accelerators. Since this procedure modifies the CMF EoS only at high densities, it leaves the low-density description consistent with nuclear matter properties and lattice QCD constraints. The resulting average field energy per baryon used for the CMF and PT1 as well as PT2 EoS are shown as orange, green and purple lines in panel (a) of figure 1. Here, the explicitly visible additional minima of the field energy leads to the presence of two coexisting different-density states.

Let us stress that the current investigation does not employ an explicit change of the dynamical degrees of freedom from hadrons to quarks, but incorporates the effects of the phase transition in the EoS on the dynamics of the system. Therefore, any effects that would specifically depend on the deconfinement aspects of the transition will not be included in the transport simulation; however, they can be included in the coarse-graining procedure. In case

of a crossover transition in a mean-field approach, a possible solution for changing the degrees of freedom has been presented in [46].

To have a better understanding of the expected influence of the modified potential on the phase structure, phase diagrams of the two CMF-PT models in the thermodynamic limit are constructed and shown in panel (b) of figure 1. The spinodal lines [33], boundaries of regions where matter becomes mechanically unstable, are defined by the densities at which the isothermal speed of sound becomes imaginary. The pressure as well as the chemical potential at given  $(n_B, T)$  can be calculated using the single-particle energy:

$$U(n_B) = \frac{\partial(n_B \cdot V(n_B))}{\partial n_B}, \quad (2)$$

$$\mu(n_B) = \mu_{\text{id}}(n_B) - U(n_B), \quad (3)$$

$$P(n_B, T) = P_{\text{id}}(n_B, T) + \int_0^{n_B} n' \frac{\partial U(n')}{\partial n'} dn'. \quad (4)$$

where  $P_{\text{id}}(n_B, T)$  and  $\mu_{\text{id}}(n_B)$  are the pressure and chemical potential of an ideal hadron resonance gas. Having calculated the pressure one can define the spinodal lines, which are shown as dashed lines in figure 1. The shaded areas are the spinodal regions of the corresponding EoS. Note that the phase transitions implemented in this work are rather strong and since we did not consider any explicit temperature dependence of the potential, there is no critical endpoint present at any finite temperature in both cases.

We would like to clarify that the QMD approach solves an interacting many-body system and is not a mean-field solution. It is true that the particular density-dependent potential used in the solution of the molecular dynamics equations of motion can be related to thermodynamics quantities in the mean-field approximation, which is what we do if we calculate the pressure and/or speed of sound of the system, as shown in [34, 44], for example. The CMF model that was used to construct the density-dependent potential is also based on a mean-field approximation. However, as we have discussed, in principle any density EoS is possible.

Panel (b) of figure 1 also includes the averaged trajectories of the central cell for central collisions at different beam energies, obtained by the coarse-graining method described below. In all three cases, the nature of the nuclear liquid–gas transition is not changed and is shown as the gray shaded area. The trajectories are shown only after the point of highest compression is reached, during the compression of the colliding nuclei, which is a direct result of the stiffness of the EoS. At the lowest beam energies the maximally reached compression in the CMF and PT2 cases is similar, whereas in the PT1 case one reaches much larger densities due to the phase separation. At the highest energy, the effect of the transition for PT1 is already much less significant, since the maximum compression is beyond the spinodal region. Therefore, we would expect to see effects of the phase transition for PT1 already at the lowest beam energy, while effects for PT2 should show up for  $E_{\text{lab}} = 2$  AGeV. In addition, the softening will also lead to a prolonged lifetime of the system and thus larger dilepton emission, as has been shown recently in a fluid dynamic simulation [28]. In the following, we study whether such a signal survives the bulk evolution in a fully microscopic non-equilibrium model. The effects of the bulk viscosity [47] do not change the lifetime of the system significantly, as can be seen from the extended lifetime, which only appears in the simulation with a phase transition. A recent study also shows the formation of density clumps only in the presence of a phase transition [48]. We observe an almost EoS-independent pion multiplicity, which indicates no significant additional entropy production [49].

## 2.2. Coarse graining

To calculate the dilepton emission during the collision, a coarse-graining approach will be employed. This approach was used in [50–60] to extract the properties of the medium from microscopic transport simulations. For this procedure, 50 000 events of the most central ( $b < 2$  fm) Au–Au collisions are simulated for several beam energies, using either of the three EoS introduced above. To calculate the medium properties, an ensemble average of the local energy and baryon densities is calculated on a space-time grid with  $\Delta x, \Delta y, \Delta z, \Delta ct = 0.5$  fm. The grid constitutes  $(100)^4$  cells spanning  $-25 < x$  [fm]  $< 25$  in space and  $0 < t$  [fm/c]  $< 50$  in time. This allows one to incorporate most (if not all) of the system created in Au–Au collisions at energies  $E_{\text{lab}} = 1 - 10$  AGeV.

The medium properties, i.e. the baryon density and temperature, can be extracted from the CMF EoS only in the local rest frame of each gridpoint. Therefore, the local flow velocity  $u = \gamma(1, \vec{v})$  has to be calculated using the ideal fluid equilibrium stress-energy tensor:

$$T^{\mu\nu} = (\varepsilon + P)u^\mu u^\nu - Pg^{\mu\nu}, \quad (5)$$

and the 0th component of baryon current:

$$N_B^0 = \gamma n_B, \quad (6)$$

where  $\varepsilon, n_B, P$  are the energy and baryon densities and pressure in the co-moving frame. Using the kinetic energy, momentum and baryon densities extracted from the coarse-grained UrQMD simulations and the pressure from the EoS, the local rest frame properties  $n_B$  and  $T$  can be found using a fixed-point iterative method used also in ideal fluid dynamical simulations [61].<sup>10</sup> There are several options on how to define the local co-moving frame either as the Landau frame or the Eckart frame, which differ in second-order viscous fluid dynamics [62]. Both definitions have been used in previous implementations of the coarse-graining procedure and no significant differences have been observed [50, 51, 53–60]. This is likely due to the fact that small differences in the flow velocity do not translate into significant changes in the overall dilepton emission. In order to self-consistently extract the temperature using the CMF model in the non-ideal hydrodynamics scenario, one would not only need to include the full CMF fields (vector and scalar) in UrQMD simulation but also transport coefficients in order to properly deal with the off-diagonal elements [63]. This is something that requires a proper covariant description of the QMD simulation, and will be discussed in future works. We have estimated that using the energy-momentum tensor extracted from UrQMD, as described in the text, and matching this to the CMF EoS will give temperatures that differ only by less than 2% from the ‘correct’ equilibrium temperature if the full fields are taken into account.

Note that we do not employ the coarse-graining method for the early stage of the collision when the system is far away from thermal equilibrium. Though the relaxation time is predicted to be smaller than the interpenetration time [28], the emission of dileptons in the very early stages of collisions is often not considered because of this uncertainty. On the other hand, a recent study has shown that shortly after interpenetration, the systems described do reach a state of local isotropy and equilibrium, and the assumption of a near-hydro  $T^{\mu\nu}$  is justified [64]. In addition to extracting the local density and temperature, the coarse-graining procedure allows the local densities of  $\pi$  and  $\rho$  mesons and  $\Delta$  baryons to be determined, which can be used to check whether a system is in local chemical equilibrium.

<sup>10</sup> Note that in this method the extracted temperature depends on the EoS used. This can lead to the underlying degrees of freedom not being the same as in the microscopic simulation.



It was found that the pion multiplicity  $n_\pi$  quickly exceeds the statistical model prediction of an ideal pion gas at a given temperature  $n_\pi^{\text{id}}(T)$  by a factor

$$\lambda_\pi = \frac{n_\pi}{n_\pi^{\text{id}}(T)}, \quad (7)$$

which can be referred to as pion fugacity. To take into account the pion number excess, the values of  $\lambda_\pi$  are used in calculations of the dilepton emissivity.

### 2.3. Dilepton emissivity

Once the system's space-time evolution is known from the coarse-graining, the emitted dileptons and their spectra as a function of the pair invariant mass  $M$  and pair momentum  $k$  can be inferred from the emission rate:

$$\frac{d^8N}{d^4x d^4k} = -\lambda_\pi^{1.3} \frac{\alpha^2}{\pi^3 M^2} f^{BE}(k^0, T) \frac{1}{3} g^{\mu\nu} \text{Im} [\Pi_{EM}^{\mu\nu}(M, k, n_B, T)], \quad (8)$$

where  $\alpha$  is the fine structure constant, and the power of 1.3 [55, 57] for the pion fugacity comes from the fact that not only pions and the  $\rho$  meson, but also direct decays from other resonances that contain one or more pions will contribute to the dilepton emissivity. The fugacity effects on the  $\rho$  and  $\omega$  mesons are assumed to be similar. Additional investigations are required to determine the precise values of the exponents. However, our main conclusions will involve parts of the spectra outside of the two peaks. The in-medium properties enter through the spectral function  $\Pi_{EM}^{\mu\nu}(M, k, n_B, T)$ , where  $n_B$  and  $T$  are the co-moving frame baryon density and temperature.

In the present work, we use the most recent version of the Rapp–Wambach–van Hees spectral function as introduced in [65–67]. This spectral function describes the EM properties of hot and dense matter calculated from the in-medium  $\rho$ ,  $\omega$  and  $\phi$  meson spectral functions from hadronic many-body theory [22], supplemented by a four-pion continuum with chiral mixing at masses above 1 GeV. We assume that most other sources of dilepton emission, e.g. late-stage hadronic contributions, like the final decays of the  $\pi^0$ ,  $\eta$ ,  $\omega$  and  $\phi$  mesons (often referred to as 'cocktail' contributions) as well as very early time emission, can be subtracted from the experimental measurements as was done in the NA60 and HADES experiments, for example. Therefore, we only simulate the dilepton yield, which carries information from the hot and dense phase, i.e. the in-medium  $\rho$ ,  $\omega$  and  $\phi$  channels. Figure 2 shows the spectral functions of all three included vector mesons in the vacuum (solid line) and in the medium (dashed line). The in-medium spectral function is shown at a temperature of  $T=120$  MeV and three times saturation density, which is representative of the systems created in the energy range we study. The  $\rho$  meson shows the strongest broadening, while  $\omega$  and  $\phi$  are also broadened in the medium. Interestingly, the in-medium  $\omega$  appears similar to a vacuum  $\rho$ , which means one can easily misinterpret the small peak in the measured dilepton spectrum for a  $\rho$ , while it in fact originates from the  $\omega$ .

It should also be noted that this in-medium rate becomes more similar to a pure quark rate as the temperature or density is increased, which is a consequence of the quark–hadron duality near the deconfinement transition. This also means that the spectral function is in principle also valid for densities above the deconfinement transition, and thus allows us to make realistic predictions on the effect of the phase transition. Further explicit effects on the spectral function, e.g. from a chiral critical point [68] or diquark fluctuations [69], are not part of this work.



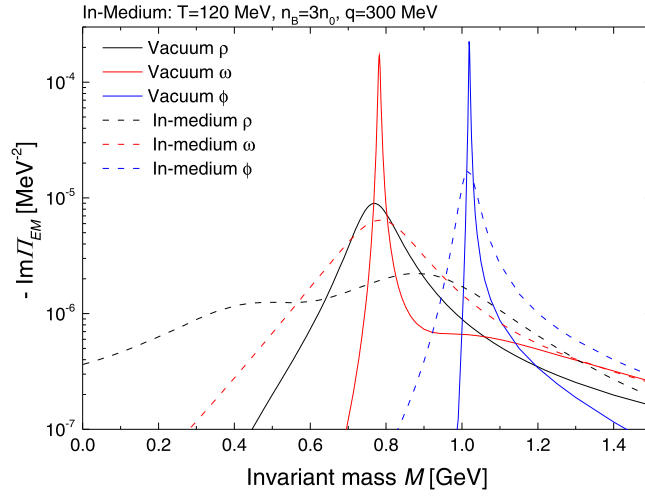


**Figure 2.** Spectral functions of the  $\rho$  (black),  $\omega$  (red) and  $\phi$  (blue) vector mesons, as a function of their invariant mass. The vacuum spectral functions (solid lines) are compared to a specific choice of in-medium spectral functions at a temperature  $T = 120$  MeV, baryon density  $n_B = 3n_0$  and momentum of pair  $q = 300$  MeV. The  $\rho$  meson shows the strongest broadening, while  $\omega$  and  $\phi$  are also broadened in the medium.

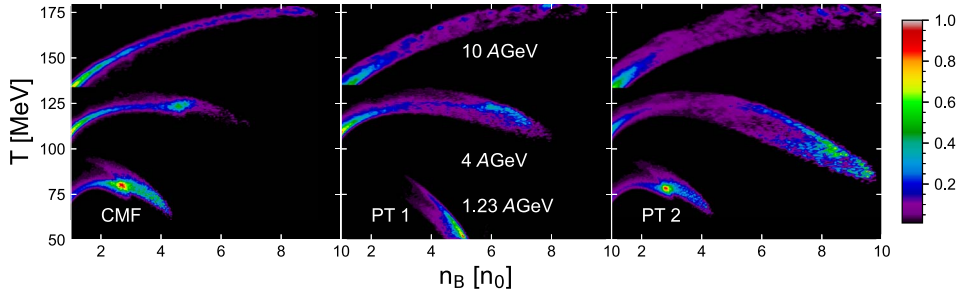


**Figure 3.** Time-integrated dilepton emission  $1/N_{ll}^{\max} d^2N_{ll}/dT dn_B$ , normalized to its maximum value  $N_{ll}^{\max}$ , for central Au–Au collisions and the three different EoS and three different beam energies. The results are calculated using the coarse-graining approach. The emission is shown as a function of temperature and density, highlighting the regions in the phase diagram that contribute most to the total dilepton excess. Clear differences between the EoS can be observed, especially if the system expands through or near the expected phase transition.

To understand and interpret the resulting dilepton spectra and yields, it is instructive to look first at the regions in the phase diagram where the dileptons are emitted in the three different scenarios. Figure 3 shows the normalized emission rate as a function of the baryon density and temperature for the CMF, as well as PT1 and PT2 EoS (from left to right). For each EoS, three separate beam energies are presented:  $E_{\text{lab}} = 1.23, 4$  and  $10$  AGeV, from bottom to top. One can clearly observe that once the system undergoes the phase transition and/or softening of the EoS, the emission at high baryon densities increases. This occurs for PT1 already at  $1.23$  AGeV and for PT2 at  $4$  AGeV. Therefore, for the case of a phase

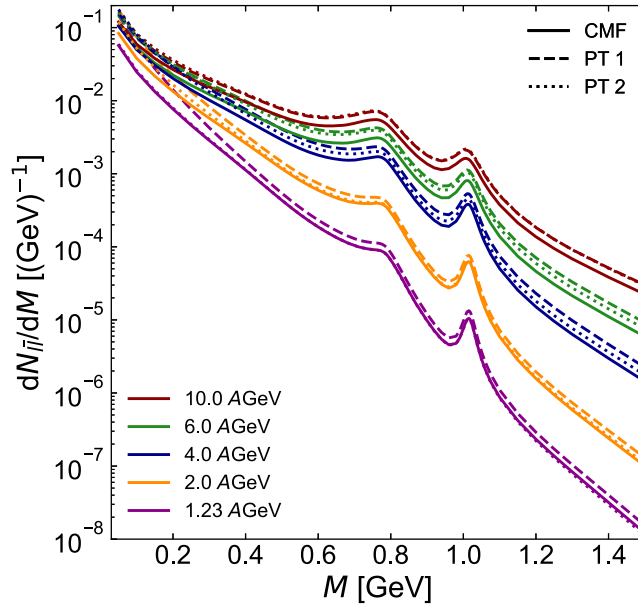


**Figure 4.** Invariant mass dilepton spectra in central Au–Au collisions calculated using the CMF and the two CMF-PT EoS for energies available in SIS18 and in the future SIS100 accelerator. Changes in the hadronic in-medium spectral function can be observed from 1.23 to 10 AGeV.

transition, we would expect an increased dilepton emission and possible increase of the extracted dilepton temperature at those beam energies.

### 3. Results

The time and momentum integrated (excess) invariant mass spectra of dileptons for central Au–Au collisions at five different beam energies, calculated with the hadronic in-medium spectral function, are presented in figure 4. Here, the CMF EoS (solid lines) is compared to the two phase transition scenarios PT1 (dashed lines) and PT2 (dotted lines).

Besides the peaks for the  $\omega$  and  $\phi$  mesons, the spectrum is very flat and no explicit  $\rho$  peak can be observed. A slight broadening of the two vector mesons is observed with the increase in beam energy, and thus the increase in the system density. Importantly, a systematic enhancement of the spectra as a result of the phase transition is observed.

To get a better quantitative understanding of the effect of the phase transitions, the inverse slope as well as the integrated yields can be useful tools. Thus, figure 5 shows the dilepton temperature, extracted from an exponential fit to the invariant mass distribution in two mass ranges,  $0.3 < M < 0.5$  GeV (solid lines) and  $1.2 < M < 1.5$  GeV (dashed lines) as functions of the beam energy. These mass ranges have been selected to avoid any contamination of  $\omega$  and  $\phi$  in the fit. As expected, the low-mass range shows a lower temperature than the intermediate-mass range, and the extracted temperature is increasing monotonically with the beam energy. The effects of the phase transition are essentially not visible in the intermediate-mass range. However, the low-mass range is more sensitive. A decrease in the temperature is observed for PT1 and PT2 at beam energies when the system passes through the unstable

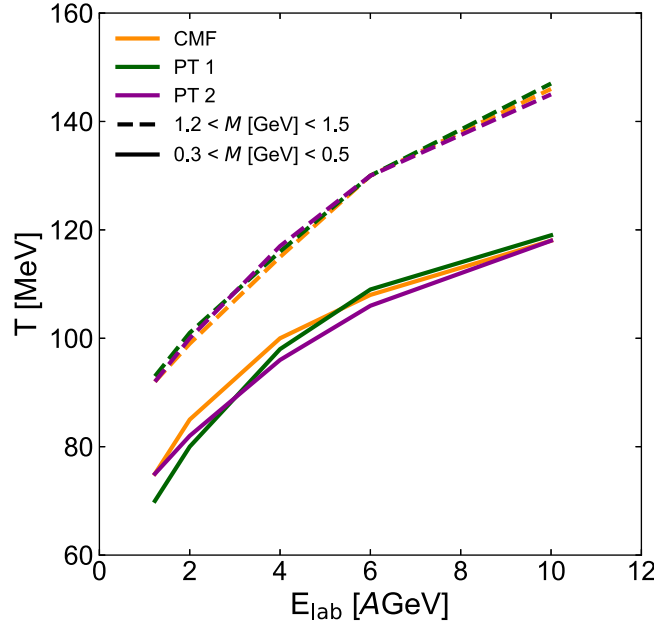


**Figure 5.** Excitation function of the dilepton temperature, extracted through exponential fits to the mid-rapidity dilepton invariant mass spectrum in two different mass ranges. The low-mass range shows a lower temperature and a stronger sensitivity to the existence of a phase transition.

region, which leads the system to emit slightly longer at a lower temperature. The observed effect corresponds to only a few MeV in temperature and thus would need a very precise experimental determination of the temperature to be used as a signal.

Finally, figure 6 shows the excitation function of the dilepton emission rate (upper panel) as well as the mid-rapidity dilepton yield integrated over the mass range  $0.3 < M < 0.7$  GeV (lower panel), both normalized by the  $dN/dy|_{y=0}$  of charged pions, for the three EoS. The strongest enhancement is observed for the dilepton emission rate  $dN_{ll}/dM$  at low masses ( $M = 50$  MeV). Here, an enhancement factor of 2–3 can be observed as soon as the created system enters the unstable region of the phase transition. This also corresponds to the beam energy where the effect is maximal, i.e. one can expect a maximum in the excitation function of the rate at that low mass as a function of the beam energy.

A clear enhancement of the normalized yield is also visible for both EoS with a phase transition.<sup>11</sup> While for PT1 the enhancement is already significant at the lowest beam energy, as here the coexistence phase is already reached, for PT2 the enhancement occurs at higher beam energies. PT1 even shows a maximum enhancement, compared to the CMF EoS, at approximately  $E_{\text{lab}} = 6$  A GeV, when the system's maximal compression is significantly above the spinodal region and the phase transition effect becomes weaker. For PT2, the dilepton excess increases up to the highest beam energy under investigation. However, we also expect to see a maximum at even higher beam energy, especially of a phase transition with a critical endpoint.

<sup>11</sup> Note that we have checked that this increase is genuinely due to an increase of the dilepton yield and that the final pion number is almost unaffected by the EoS.

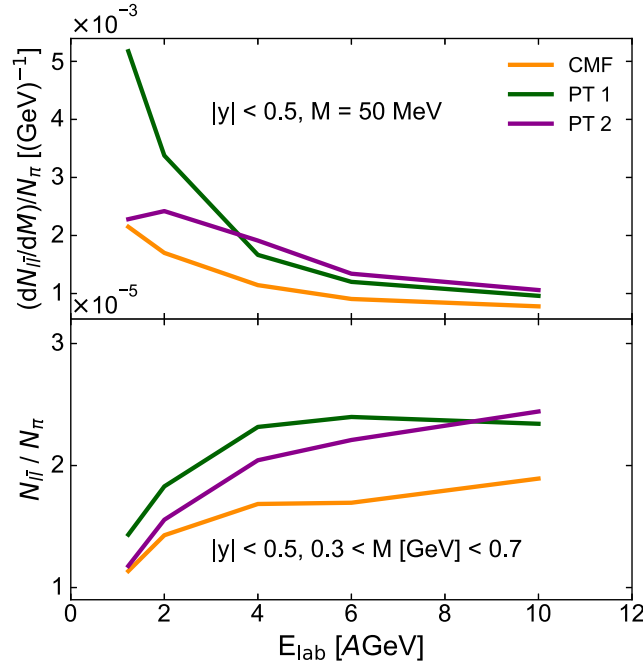


**Figure 6.** Upper panel: Dilepton emission rate  $dN_{l\bar{l}}/dM$  at  $M = 50$  MeV, integrated over all momenta at mid-rapidity and normalized by the charged pion yield as a function of the projectile kinetic beam energy. At this low mass the enhancement of the emission rate is very strong if a phase transition is reached. The maximum enhancement occurs at the beam energy when the system enters the phase transition. Lower panel: Integrated dilepton yield over charged pion number in one unit of rapidity, at mid-rapidity, as functions of the projectile kinetic beam energy. The dileptons are integrated in the low-mass range of the invariant mass distribution. One can observe a clear and significant increase of the dilepton yield once the phase transition (or significant softening) is reached. The maximum in the enhancement is reached only once the initial compression has clearly surpassed the phase transition coexistence densities.

One would expect that relativistic effects become more relevant as the beam energies increase from 1 to 10 AGeV [70–77]. Their treatment requires a relativistic reformulation of the current approach. To a certain degree this has been done within the RQMD model, which requires not only the vector but also scalar density-dependent potentials as an input. How a phase transition in both scalar and vector density can be properly and consistently implemented is still to be resolved and will be the focus of future work. The qualitative effects of a slower evolution, i.e. longer lifetime, should be independent of having a relativistic or non-relativistic description, and thus the conclusions of our paper are expected to be robust, even though further developments to understand the quantitative effects are certainly in order.

#### 4. Conclusions

It was shown that a first-order phase transition in a dynamical non-equilibrium transport description of HICs will lead to a significant enhancement in the measured dilepton yield at low invariant mass and low beam energies per charged pion. Unlike previous studies, in this

setup, the whole evolution is treated within a consistent dynamical framework that allows us to describe particle production as well as the dynamical evolution of the system without the introduction of additional parameters. In addition, since we use a microscopic transport model, the effects of finite viscosity and a finite system size are naturally included. The different magnitude of the signal, as compared to [28], can be understood as a result of the finite viscosity as well as a different treatment of the effective degrees of freedom in the coarse-graining procedure as compared to the hydro approach.

The predicted enhancement factor of 2–3 for the emission rate at masses of  $M \approx 50$  MeV and 1.5 from the integrated yield in the whole low-mass region is still sizeable enough to be measured by the upcoming experiments.

In addition, a dilepton temperature reduction of about 5 MeV is observed in the low-mass range when the system created in the nuclear collision reaches densities in the coexistence region of the transition.

## Acknowledgments

The authors thank L Satarov, H Stöcker, R Rapp and J Stroth for their fruitful comments and discussions. OS acknowledges the scholarship grant from the GET\_INvolved Programme of FAIR/GSI. AM acknowledges the Stern–Gerlach Postdoctoral Fellowship of the Stiftung Polytechnische Gesellschaft. JS thanks the Samson AG and the BMBF through ErUM-Data for funding. This article is part of a project that has received funding from the European Union's Horizon 2020 research and innovation programme under grant agreement STRONG2020—No. 824 093. This work is supported by the National Academy of Sciences of Ukraine, Grant No. 0122U200259. VV was supported through the U.S. Department of Energy, Office of Science, Office of Nuclear Physics, under contract number DE-FG02-00ER41132. MIG acknowledges the support from the Alexander von Humboldt Foundation. TG acknowledges the support by the State of Hesse within the Research Cluster ELEMENTS (Project ID 500/10.006).

## Data availability statement

The data cannot be made publicly available upon publication because no suitable repository exists for hosting data in this field of study. The data that support the findings of this study are available upon reasonable request from the authors.

## ORCID iDs

Oleh Savchuk  <https://orcid.org/0000-0003-0141-0610>

Anton Motornenko  <https://orcid.org/0000-0003-3037-9923>

Jan Steinheimer  <https://orcid.org/0000-0003-2565-7503>

Volodymyr Vovchenko  <https://orcid.org/0000-0002-2189-4766>

## References

- [1] Abbott B P *et al* (LIGO Scientific, Virgo) 2017 *Phys. Rev. Lett.* **119** 161101
- [2] Abbott B P *et al* (LIGO Scientific, Virgo) 2020 *Astrophys. J. Lett.* **892** L3
- [3] Borsanyi S, Fodor Z, Hoelbling C, Katz S D, Krieg S and Szabo K K 2014 *Phys. Lett. B* **730** 99
- [4] Bazavov A *et al* (HotQCD) 2014 *Phys. Rev. D* **90** 094503

- [5] Bazavov A *et al* 2017 *Phys. Rev. D* **95** 054504
- [6] Bzdak A, Esumi S, Koch V, Liao J, Stephanov M and Xu N 2020 *Phys. Rept.* **853** 1
- [7] Acharya S *et al* (ALICE) 2020 *Phys. Lett. B* **807** 135564
- [8] Abdallah M *et al* (STAR) 2021 *Phys. Rev. C* **104** 024902
- [9] Abdallah M *et al* (STAR) 2021 *Phys. Rev. Lett.* **127** 262301
- [10] Rischke D H, Pürsün Y, Maruhn J A, Stoecker H and Greiner W 1995 *Acta Phys. Hung. A* **1** 309
- [11] Stoecker H 2005 *Nucl. Phys. A* **750** 121
- [12] Brachmann J, Soff S, Dumitru A, Stoecker H, Maruhn J A, Greiner W, Bravina L V and Rischke D H 2000 *Phys. Rev. C* **61** 024909
- [13] Brachmann J, Dumitru A, Stoecker H and Greiner W 2000 *Eur. Phys. J. A* **8** 549
- [14] Stephanov M A, Rajagopal K and Shuryak E V 1998 *Phys. Rev. Lett.* **81** 4816
- [15] Stephanov M A, Rajagopal K and Shuryak E V 1999 *Phys. Rev. D* **60** 114028
- [16] Jeon S and Koch V 2000 *Phys. Rev. Lett.* **85** 2076
- [17] Asakawa M, Heinz U W and Muller B 2000 *Phys. Rev. Lett.* **85** 2072
- [18] Sun K-J, Chen L-W, Ko C M and Xu Z 2017 *Phys. Lett. B* **774** 103
- [19] Shuryak E V 1978 *Phys. Lett. B* **78** 150
- [20] McLerran L D and Toimela T 1985 *Phys. Rev. D* **31** 545
- [21] Bratkovskaya E L and Cassing W 1997 *Nucl. Phys. A* **619** 413
- [22] Rapp R and Wambach J 2000 *Adv. Nucl. Phys.* **25** 1
- [23] Rapp R and van Hees H 2016 *Phys. Lett. B* **753** 586
- [24] Santini E, Steinheimer J, Bleicher M and Schramm S 2011 *Phys. Rev. C* **84** 014901
- [25] Li F and Ko C M 2017 *Phys. Rev. C* **95** 055203
- [26] Heinz U W and Lee K S 1991 *Phys. Lett. C* **259** 162
- [27] Rischke D H and Gyulassy M 1996 *Nucl. Phys. A* **608** 479
- [28] Seck F, Galatyuk T, Mukherjee A, Rapp R, Steinheimer J and Stroth J 2022 *Phys. Rev. C* **106** 014904
- [29] Bauchle B and Bleicher M 2011 *Phys. Lett. B* **695** 489
- [30] Bass S A *et al* 1998 *Prog. Part. Nucl. Phys.* **41** 255
- [31] Bleicher M *et al* 1999 *J. Phys. G* **25** 1859
- [32] Bleicher M and Bratkovskaya E 2022 *Prog. Part. Nucl. Phys.* **122** 103920
- [33] Savchuk O, Vovchenko V, Poberezhnyuk R V, Gorenstein M I and Stoecker H 2020 *Phys. Rev. C* **101** 035205
- [34] Omana Kuttan M, Motornenko A, Steinheimer J, Stoecker H, Nara Y and Bleicher M 2022 *Eur. Phys. J. C* **82** 427
- [35] Vogel S, Petersen H, Schmidt K, Santini E, Sturm C, Aichelin J and Bleicher M 2008 *Phys. Rev. C* **78** 044909
- [36] Schmidt K, Santini E, Vogel S, Sturm C, Bleicher M and Stocker H 2009 *Phys. Rev. C* **79** 064908
- [37] Bratkovskaya E L, Aichelin J, Thomere M, Vogel S and Bleicher M 2013 *Phys. Rev. C* **87** 064907
- [38] Oliinychenko D, Shen C and Koch (SMASH) V 2021 *Phys. Rev. C* **103** 034913
- [39] Staudenmaier J, Oliinychenko D, Torres-Rincon J M and Elfner (SMASH) H 2021 *Phys. Rev. C* **104** 034908
- [40] Steinheimer J, Motornenko A, Sorensen A, Nara Y, Koch V and Bleicher M 2022 *arXiv:2208.12091*
- [41] Motornenko A, Steinheimer J, Vovchenko V, Schramm S and Stoecker H 2020 *Phys. Rev. C* **101** 034904
- [42] Aichelin J 1991 *Phys. Rept.* **202** 233
- [43] Huth S *et al* 2022 *Nature* **606** 276
- [44] Li P, Steinheimer J, Reichert T, Kittiratpattana A, Bleicher M and Li Q 2023 *Sci. China Phys. Mech. Astron.* **66** 232011
- [45] Sorensen A and Koch V 2021 *Phys. Rev. C* **104** 034904
- [46] Cassing W and Bratkovskaya E 2009 *Nucl. Phys. A* **831** 215
- [47] Denicol G S, Gale C and Jeon S 2015 The domain of validity of fluid dynamics and the onset of cavitation in ultrarelativistic heavy ion collisions <https://arxiv.org/pdf/1503.00531.pdf>
- [48] Savchuk O, Poberezhnyuk R V, Motornenko A, Steinheimer J, Gorenstein M I and Vovchenko V 2023 *Phys. Rev. C* **107** 10.1103
- [49] Vujanovic G, Paquet J-F, Shen C, Denicol G S, Jeon S, Gale C and Heinz U 2020 *Phys. Rev. C* **101** 10.1103
- [50] Bravina L V *et al* 1998 *Phys. Lett. B* **434** 379

- [51] Bravina L V *et al* 1999 *Phys. Rev. C* **60** 024904
- [52] Huovinen P, Belkacem M, Ellis P J and Kapusta J I 2002 *Phys. Rev. C* **66** 014903
- [53] Endres S, van Hees H and Bleicher M 2013 *PoS CPOD2013* 052
- [54] Endres S, van Hees H, Weil J and Bleicher M 2015 *Phys. Rev. C* **91** 054911
- [55] Endres S, van Hees H, Weil J and Bleicher M 2015 *Phys. Rev. C* **92** 014911
- [56] Endres S, van Hees H and Bleicher M 2016 *Phys. Rev. C* **93** 054901
- [57] Galatyuk T, Hohler P M, Rapp R, Seck F and Stroth J 2016 *Eur. Phys. J. A* **52** 131
- [58] Endres S, van Hees H and Bleicher M 2016 *Phys. Rev. C* **94** 024912
- [59] Reichert T, Inghirami G and Bleicher M 2020 *Eur. Phys. J. A* **56** 267
- [60] Reichert T, Inghirami G and Bleicher M 2021 *Phys. Lett. B* **817** 136285
- [61] Rischke D H, Bernard S and Maruhn J A 1995 *Nucl. Phys. A* **595** 346
- [62] Monnai A 2019 *Phys. Rev. C* **100** 014901
- [63] Denicol G S, Molnár E, Niemi H and Rischke D H 2012 *Eur. Phys. J. A* **48** 170
- [64] Inghirami G and Elfner H 2022 *Eur. Phys. J. C* **82** 796
- [65] Rapp R and Wambach J 1999 *Eur. Phys. J. A* **6** 415
- [66] van Hees H and Rapp R 2008 *Nucl. Phys. A* **806** 339
- [67] Rapp R 2013 *Adv. High Energy Phys.* **2013** 148253
- [68] Tripolt R-A, Jung C, Tanji N, von Smekal L and Wambach J 2019 *Nucl. Phys. A* **982** 775
- [69] Nishimura T, Kitazawa M and Kunihiro T 2022 arXiv:2201.01963
- [70] Ko C M, Li Q and Wang R-C 1987 *Phys. Rev. Lett.* **59** 1084
- [71] Ko C-M and Li Q 1988 *Phys. Rev. C* **37** 2270
- [72] Blattel B, Koch V, Cassing W and Mosel U 1988 *Phys. Rev. C* **38** 1767
- [73] Sorge H, Stoecker H and Greiner W 1989 *Annals Phys.* **192** 266
- [74] Blaettel B, Koch V and Mosel U 1993 *Rept. Prog. Phys.* **56** 1
- [75] Fuchs C, Lehmann E, Sehn L, Scholz F, Kubo T, Zipprich J and Faessler A 1996 *Nucl. Phys. A* **603** 471
- [76] Buss O, Gaitanos T, Gallmeister K, van Hees H, Kaskulov M, Lalakulich O, Larionov A B, Leitner T, Weil J and Mosel U 2012 *Phys. Rept.* **512** 1
- [77] Nara Y and Stoecker H 2019 *Phys. Rev. C* **100** 054902